Imaging Transverse Isotropic Properties of Muscle by Monitoring Acoustic Radiation Force Induced Shear Waves Using a 2-D Matrix Ultrasound Array

Michael Wang*, *Member, IEEE*, Brett Byram, *Member, IEEE*, Mark Palmeri, *Member, IEEE*, Ned Rouze, *Member, IEEE*, and Kathryn Nightingale, *Member, IEEE*

Abstract—A 2-D matrix ultrasound array is used to monitor acoustic radiation force impulse (ARFI) induced shear wave propagation in 3-D in excised canine muscle. From a single acquisition, both the shear wave phase and group velocity can be calculated to estimate the shear wave speed (SWS) along and across the fibers, as well as the fiber orientation in 3-D. The true fiber orientation found using the 3-D radon transform on B-mode volumes of the muscle was used to verify the fiber direction estimated from shear wave data. For the simplified imaging case when the ARFI push can be oriented perpendicular to the fibers, the error in estimating the fiber orientation using phase and group velocity measurements was $3.5 \pm 2.6°$ and $3.4 \pm 1.4°$ (mean ± standard deviation), respectively, over six acquisitions in different muscle samples. For the more general case when the push is oblique to the fibers, the angle between the push and the fibers is found using the dominant orientation of the shear wave displacement magnitude. In 30 acquisitions on six different muscle samples with oblique push angles up to 40°, the error in the estimated fiber orientation using phase and group velocity measurements was $5.4 \pm 2.9°$ and $5.3 \pm 3.2°$, respectively, after estimating and accounting for the additional unknown push angle. Either the phase or group velocity measurements can be used to estimate fiber orientation and SWS along and across the fibers. Although it is possible to perform these measurements when the push is not perpendicular to the fibers, highly oblique push angles induce lower shear wave amplitudes which can cause inaccurate SWS measurements.

Index Terms—Acoustic radiation force, elastography, shear wave imaging, transverse isotropy, ultrasound.

I. INTRODUCTION

SHEAR wave imaging is a promising technique for the noninvasive quantification of tissue stiffness. Shear waves in the body can be induced by a variety of methods, including physiological motion [1]–[4], external mechanical excitation [5]–[7], or acoustic radiation force [8]–[11]. By monitoring the shear wave speed (SWS) using a real-time imaging modality such as magnetic resonance imaging (MRI) [5], [6], [12] or

ultrasound [7]–[11], the underlying tissue stiffness can be estimated under simplifying assumptions of the tissue mechanical properties. This technique has been used to study various types of soft tissues, including liver [5], [7], [13]–[15], breast [16], [17], cardiac tissue [1], [18], [19], skeletal muscle [20], [21], artery [2], kidney [22], cornea [23], and brain [24]–[26].

Shear wave imaging in skeletal muscle presents unique challenges due to its dynamic nature and its physical structure. Skeletal muscle is composed of thin fibers (myocytes) grouped together in bundles called fasciculi [27]. These fibers align parallel to each other in a regularized pattern to form the overall muscle. Due to this geometric structure, the mechanical properties of muscle are different along the fibers than across the fibers. As a result, the SWS in muscle is anisotropic, and dependent on the direction of propagation with respect to the fiber orientation, which confounds SWS measurement in muscle in two ways. First, the muscle fiber orientation is not usually precisely known in the shear wave imaging coordinate system. Second, the usual assumption of isotropy used in SWS based shear modulus reconstruction techniques does not apply.

Previous work in shear wave imaging in muscle includes both magnetic resonance elastography (MRE) studies, which use MRI for monitoring shear waves, and ultrasound-based techniques. MRI has the advantages of being able to acquire data in 3-D and measure displacement fields with equal sensitivity in any direction. However, the long acquisition time required (on the order of minutes) means that most MRE studies are limited to data from a single 2-D plane of the anatomy [21], [28], [29]. Another drawback of MRE is the complexity of wave fields induced in muscle by the external mechanical vibrators typically used for shear wave generation [30]–[32], which make the reconstruction of elastic parameters a challenging task. At present, the majority of MRE studies measure muscle stiffness only in the fiber direction [28], [29], [32], [33], while assessments of anisotropy are limited [21], [31].

In comparison to MRI, the use of ultrasound for shear wave imaging has several advantages, including short acquisition times (within seconds), portability, reduced cost, and the ability to generate shear waves in tissue using acoustic radiation force with the imaging transducer [11]. Early studies in muscle with ultrasound-based shear wave imaging were performed using mechanical actuators for shear wave generation [10], [34]–[36], and more recently with acoustic radiation force [20], [37]. However, like most MRE techniques, shear wave propagation

in only a single plane can be observed using conventional ultrasound, which form cross-sectional image slices. This limits its ability to characterize the anisotropic properties of muscle, which is 3-D in nature. Some studies seek to minimize the effect of anisotropy on SWS measurements in muscle by consistently orienting the transducer imaging plane with respect to the fiber and limiting measurements to a single direction [35], [36]. In other studies, anisotropy has been characterized by modulating either the excitation source of the shear wave [34], [38], or the position of the imaging transducer [20]. A common drawback in these approaches is that the actual fiber orientation relative to the imaging plane is not known precisely, and is estimated by manual inspection of the appearance of fasciculi in B-mode. More recently, Lee *et al.* [18] have shown that it is possible to accurately estimate the fiber orientation in the myocardium from the SWS measured in multiple directions using a transducer mounted on a custom rotation device.

Two-dimensional matrix array ultrasound transducers are becoming increasingly available on the latest generation commercial ultrasound scanners. In contrast to conventional 1-D ultrasound arrays, these transducers are capable of electronic beamforming in both the lateral and elevation dimensions to facilitate 3-D imaging at high frame-rates. As a result, it is now possible to monitor shear wave propagation in a 3-D volume using ultrasound without the need for multiple acquisitions or specialized devices for repositioning and physical registration of the probe [39]. The ability to monitor shear wave propagation in 3-D overcomes the limitations inherent in characterizing muscle anisotropy from 2-D images.

In this study, a 2-D matrix array is used to image shear wave propagation induced by acoustic radiation force impulse (ARFI) in *ex vivo* muscle. The SWS along and across the fibers, as well as the fiber orientation in 3-D is measured from a single 3-D shear wave acquisition without the need to modulate the source of the shear wave or reposition the probe. Section II of this paper presents a theoretical background on shear wave propagation in muscle. Section III describes the experimental procedures used for data acquisition, methods used for anisotropic SWS estimation and fiber orientation measurement from 3-D shear wave data, as well as evaluation of the true 3-D fiber orientation from high resolution B-mode ultrasound. The 3-D fiber orientation estimated from 3-D shear wave data is compared to the true fiber orientation measured from B-mode in Section IV. It is shown that measurement of the SWS along and across the fibers, as well as the fiber orientation, is possible even when the axis of the ARFI excitation (push) is not oriented directly perpendicular to the fibers.

II. SHEAR WAVE PROPAGATION IN MUSCLE

As illustrated in Fig. 1, the parallel arrangement of muscle fibers give rise to an axis of symmetry along the fiber direction. In the coordinate system to be used throughout this paper, this axis will be assigned the three-direction ($\mathbf{e_3}$). The muscle mechanical properties are assumed to be invariant under rotation about this axis. Thus, isotropic behavior is observed in "planes of isotropy" (the 1–2 dimensions). In contrast, "planes of symmetry" parallel to this axis contain directions varying from parallel to perpendicular to the fibers, and display anisotropic behavior. This type of material symmetry can be described by a
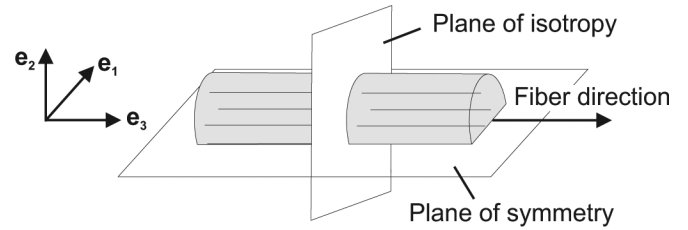

Fig. 1. Coordinate system used for modeling muscle as a transverse isotropic material. Orthonormal basis vectors $\mathbf{e_1}$, $\mathbf{e_2}$, and $\mathbf{e_3}$ form a right-handed coordinate system. Muscle fibers are parallel to the $\mathbf{e_3}$ direction, which is an axis of symmetry. Mechanical properties are isotropic within planes of isotropy perpendicular to this axis, whereas anisotropic behavior is observed in planes of symmetry parallel to this axis.

transverse isotropic (TI) model of elasticity [40]. It is the simplest model of anisotropy, and represents an attractive one to use to describe the mechanical properties of muscle [34]. The governing equations for shear wave propagation in a TI material are developed in the following subsections.

A. Wave Propagation in Transverse Isotropic Media

Wave propagation in TI materials has been extensively studied in geophysics and crystal acoustics [41], [42]. The wave equation in a TI material can be derived from three fundamental relations: 1) the strain-displacement relation, 2) the constitutive equation relating stress and strain, and 3) the equation of motion (Newton's second law). For compactness, this paper will use indicial notation, where subscript indices can take on the values 1, 2, or 3, and repeated indices follow the Einstein summation convention [40]. Let u_i denote the particle displacement in an elastic medium. The infinitesimal strain tensor ε_{kl} is then given by

$$\varepsilon_{kl} = \frac{1}{2}(u_{k,l} + u_{l,k}). \tag{1}$$

The constitutive equation for a linear elastic solid is

$$\sigma_{ij} = C_{ijkl}\varepsilon_{kl} \tag{2}$$

where σ_{ij} is the stress tensor, and C_{ijkl} is the elasticity tensor. For a TI material, the elasticity tensor contains only five independent parameters and (2) can be expressed in Voigt notation by

$$\begin{bmatrix} \sigma_{11} \\ \sigma_{22} \\ \sigma_{33} \\ \sigma_{23} \\ \sigma_{31} \\ \sigma_{12} \end{bmatrix} = \begin{bmatrix} C_{11} & C_{12} & C_{13} & & & \\ C_{12} & C_{11} & C_{13} & & & \\ C_{13} & C_{13} & C_{33} & & & \\ & & & C_{44} & & \\ & & & & C_{44} & \\ & & & & & C_{66} \end{bmatrix} \begin{bmatrix} \varepsilon_{11} \\ \varepsilon_{22} \\ \varepsilon_{33} \\ 2\varepsilon_{23} \\ 2\varepsilon_{31} \\ 2\varepsilon_{12} \end{bmatrix} \tag{3}$$

where $C_{12} = C_{11} - 2C_{66}$ and only the nonzero components are shown. The equation of motion in the absence of body forces is

$$\sigma_{ij,j} = \rho\ddot{u}_i \tag{4}$$

where $\sigma_{ij,j}$ is the divergence of the stress tensor and ρ is the material density (assumed to be 1100 kg/m^3 for muscle). The wave equation is obtained by substituting (1) and (2) into (4)

$$C_{ijkl}u_{l,kj} = \rho \ddot{u}_i. \tag{5}$$

To solve the wave equation, assume plane wave solutions of the form

$$u_i = A_i e^{j(\omega t - k_l x_l)} \tag{6}$$

where A_i are components of the particle displacement vector **A**, ω the angular frequency, t time, k_l components of the wave number vector **k**, and x_l spatial coordinates. Due to symmetry of the material properties about $\mathbf{e_3}$, the $\mathbf{e_1}$ and $\mathbf{e_2}$ directions are equivalent and arbitrary. Therefore, without any loss in generality, we can set $k_2 = 0$, and only consider wave propagation in the 1–3 plane. Substituting (6) into (5) with $k_2 = 0$ yields

$$\Gamma \mathbf{A} = \rho v_w^2 \mathbf{A} \tag{7}$$

where

$$\Gamma = \begin{bmatrix} n_1^2 C_{11} & 0 & n_1 n_3 \\ +n_3^2 C_{44} & & \times(C_{13}+C_{44}) \\ 0 & n_1^2 C_{66} & 0 \\ & +n_3^2 C_{44} & \\ n_1 n_3 & 0 & n_1^2 C_{44} \\ \times(C_{13}+C_{44}) & & +n_3^2 C_{33} \end{bmatrix} \tag{8}$$

$n_i = k_i/\sqrt{k_l k_l}$ are components of a unit vector **n** normal to the wavefront, and $v_w = \omega/\sqrt{k_l k_l}$ is the scalar phase velocity associated with the direction **n**. Equation (7) is known as Christoffel's equation, and has the form of an eigenvalue-eigenvector problem. It has three independent solutions, corresponding to three different wave-modes. The direction of particle motion **A**, or "polarization" for each wave-mode corresponds to an eigenvector of the Christoffel matrix Γ, while the phase velocity v_w can be deduced from the associated eigenvalue. It is clear from (8) that the phase velocity of the waves depend on the direction of propagation **n**, and elastic constants of the medium. Furthermore, since Γ is symmetric, the three wave-modes have mutually orthogonal directions of polarization.

One obvious solution of (7) is to set $A_1 = 0$ and $A_3 = 0$. Doing this, one obtains

$$\rho v_w^2 = n_1^2 C_{66} + n_3^2 C_{44} \quad \text{and} \quad \mathbf{A} = \gamma \begin{bmatrix} 0 & 1 & 0 \end{bmatrix}^\top \tag{9}$$

where γ is an arbitrary constant. The polarization of this wave is in the two-direction, which is perpendicular to its direction of propagation (the 1–3 plane). Thus, this mode corresponds to a pure shear wave. Equation (9) can be rewritten as

$$\rho v_w^2 = C_{66} \sin^2 \phi_w + C_{44} \cos^2 \phi_w \tag{10}$$

where $\phi_w = \arctan(n_1/n_3)$ is the angle of wave propagation with respect to the fibers in the propagation plane.

Since the three wave-modes have mutually orthogonal directions of polarization, the other two modes are obtained by set-
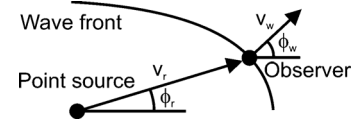

Fig. 2. Phase and group velocity measurement for a wave emitted from a point source in an anisotropic medium. Phase velocity direction (ϕ_w) is always perpendicular to the wave front, and its magnitude (v_w) corresponds to how fast a plane wave would travel in that direction. The group velocity is measured in the direction of the ray from the source to the observer (ϕ_r). Its magnitude (v_r) corresponds to how fast a wave packet consisting of plane waves in many directions would travel in that direction. Note that the vectors on this diagram indicate directions only and are not drawn to scale.

ting $A_2 = 0$ in (7). Their polarizations lie within the plane of propagation (the 1–3 plane). The expressions for the phase velocities of these two modes are algebraically complex, and the reader is referred to [41], [42] for a detailed treatment. In general, the polarization of these two wave-modes are neither purely perpendicular or parallel to the direction of propagation. The mode which has polarization closest to being perpendicular is usually referred to as the "quasi-transverse" mode, the other "quasi-longitudinal." In this study, the generation of these two wave-modes are minimized by orienting the axis of the ARFI push close to perpendicular to the muscle fibers, as will be described later. In addition, the quasi-longitudinal wave phase velocity is three orders of magnitude greater than that of a shear wave in a nearly incompressible material such as muscle, and cannot be observed using ultrasonic imaging.

B. Phase Velocity and Group Velocity in Anisotropic Media

An important concept in anisotropy is the distinction between *phase velocity* and *group velocity*. To understand the difference between them, consider a point source radiating plane waves equally in all directions in an nondispersive anisotropic medium as shown in Fig. 2. For an observer at some arbitrary location, one method to determine the velocity of the wave is by measuring its transit time between the source and the observer, and noting the distance between the two points. The velocity measured in this fashion is the group velocity, the magnitude of which we will denote by v_r (the subscript r stands for ray). It corresponds to how fast a wave packet, consisting a superposition of plane waves in different directions, would travel along the ray direction ϕ_r from the source to the observer. The polar graph of v_r *versus* ϕ_r is known as the wave surface, and represents a snapshot of the wave at unit time excited by a point source.

If, on the other hand, the location or timing of the source were unknown, it is still possible for the observer to measure a speed and a direction for the wave by comparing its arrival-times at several adjacent locations in the surrounding local domain. By limiting the observation of wave travel to a small region of space in this fashion, an individual phase of the wavefront is monitored. This is because on a sufficiently small scale, any wavefront will appear to be a plane wave. The speed measured by this method is thus the phase velocity introduced in Section II-A, the magnitude of which we have denoted by v_w, and direction by ϕ_w (the subscript w stands for wave). It corresponds to how fast a plane wave would travel in a given direction. The polar plot of

v_w versus ϕ_w is known as the velocity surface, and unlike the wave surface described above, has no simple physical interpretation.

In a nondispersive isotropic medium, the phase and group velocities are identical. However, in an anisotropic medium, the phase and group velocity magnitudes in the same direction are in general not equal. In fact, group velocities can have multiple values in the same direction, whereas the phase velocity is always a single valued function of direction [42]. In addition, at any location on a nonplanar wavefront, the phase and group velocity directions are also generally different. The phase velocity direction ϕ_w is by definition perpendicular to the wavefront, while this is not necessarily the case for the group velocity direction ϕ_r.

It is worth noting that phase and group velocity are general concepts. The differences between the two types of speed measurements can be due to any mechanism which causes the wave velocity to vary over homogeneous media. This includes dispersion due to viscosity, where the speed varies with frequency, as well as anisotropy, where the speed varies with direction. The effect of viscosity on phase velocity can be quantified using a technique such as Fourier spectroscopy [43]. This method uses the Fourier transform to separate and measure the speed of individual frequency components of a broadband shear wave. The isolation of individual plane wave components emitted by a point source as described here is an analogous concept for anisotropic media. To account for the effects of both viscosity and anisotropy in phase velocity measurements, both Fourier spectroscopy and analysis of wave propagation over small spatial domains where the wave front is locally planar can be applied concurrently. In this paper, the effects of viscosity will be neglected as a first order approximation, and the terms *phase* and *group* velocity will be used in the context of anisotropy only.

The phase velocity of shear waves in TI media was derived Section II-A and shown in (10). The group velocity may be found from the phase velocity using the transformation [42]

$$v_r = \sqrt{v_w^2 + \left(\frac{dv_w}{d\phi_w}\right)^2} \text{ and } \phi_r$$
$$= \phi_w + \arctan\left(\frac{1}{v_w}\frac{dv_w}{d\phi_w}\right). \tag{11}$$

For shear waves in TI media, substitution of (10) into (11) leads to the following expression for the group velocity:

$$\rho v_r^2 = \frac{C_{44}C_{66}}{C_{44}\sin^2\phi_r + C_{66}\cos^2\phi_r}. \tag{12}$$

The shear wave phase and group velocities parallel ($\phi_w = \phi_r = 0°$) and perpendicular ($\phi_w = \phi_r = 90°$) to the fibers are equal and are given by

$$v_w(0°) = v_r(0°) = \sqrt{\frac{C_{44}}{\rho}} \tag{13a}$$

$$v_w(90°) = v_r(90°) = \sqrt{\frac{C_{66}}{\rho}}. \tag{13b}$$

The elastic constant C_{44} is also known as the longitudinal shear modulus, and C_{66} the transverse shear modulus. The wave and velocity surfaces for a shear wave in a typical muscle-like TI material are shown in Fig. 3. As it can be seen, the wave surface is an ellipse, while the velocity surface has a figure-eight shape (mathematically known as a hippopede, or "horse-fetter" curve).

III. METHODS

It can be seen from the previous section that measurement of the SWS along and across muscle fibers allows one to quantify the TI elastic constants C_{44} and C_{66} (the longitudinal and transverse shear moduli). The following subsections will describe how the SWS along and across the fibers, as well as the 3-D fiber orientation, can be estimated by monitoring shear wave propagation using a 2-D matrix array transducer in *ex vivo* muscle samples. The methods used for independent verification of the true 3-D fiber orientation in these samples are also presented.

A. Experimental Setup

An annular focused HIFU piston transducer (H-101, Sonic Concepts, Bothell, WA, USA) was used to induce shear wave propagation with acoustic radiation force. The push was a 400 cycle, 1.1-MHz pulse with a derated intensity of $I_{SPPA.3} = 3175$ W/cm² focused at 63.2 mm axially from the radiating surface of the HIFU transducer with a F/1 focal geometry. A 2.8 MHz 2-D matrix array transducer (4Z1C on an SC2000 scanner, Siemens Healthcare, Ultrasound Business Unit, Mountain View, CA, USA) inserted in the 38.1-mm-diameter central opening of the HIFU piston was used for monitoring the resulting shear wave displacement in 3-D [44]. This transducer contains 48×36 (lateral $\times$ elevation) square elements 0.4 mm in dimension. A 72×72 (lateral $\times$ elevation) rectangular grid of tracking beams was used for shear wave tracking. At an axial depth of 60 mm in 4Z1C coordinates, which is close to the HIFU push focus when the two transducers are coupled, these beams give a 38×38 mm coronal field-of-view (FOV). The push axis was located at the center of this grid so that the SWS in all directions away from the push could be measured. 64:1 parallel receive was used to beamform a grid of 8×8 beams on every transmit so that only 81 transmits were required to interrogate the entire grid of 72×72 beams. No form of compounding was used to improve the B-mode resolution or signal-to-noise ratio. Shear wave displacement was monitored by repeating the push, and sequentially monitoring each of the 81 parallel receive beam groups in turn, until data from the entire FOV was acquired. Thus, 81 ARFI excitations in total were required to acquire data over the 3-D volume. The time interval between pushes was 22 s, and was limited by the data transfer rate on the SC2000, and not any physical ultrasonic imaging constraints. This results in a total acquisition time of 30 min for the entire FOV. A frame rate of 7.7 kHz was used to image shear wave dynamics, and the total tracking duration was 16 ms. Axial displacement along each beamline was measured using a zero-phase displacement estimation algorithm [45].
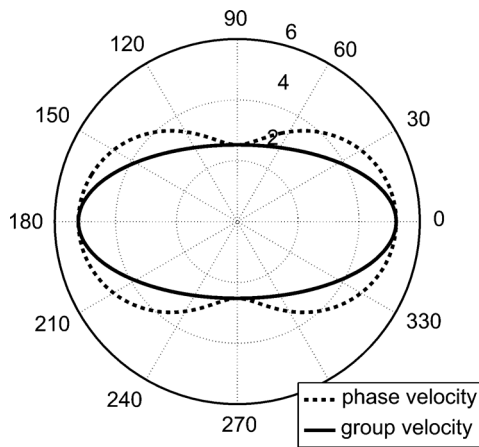
Fig. 3. The phase and group velocity [m/s] of shear waves traveling in a TI material with $C_{44} = 30$ kPa, $C_{66} = 7$ kPa, and $\rho = 1100$ kg/m^3. The wave surface (group velocity) is an ellipse, while the velocity surface (phase velocity) is a hippopede. The phase and group velocities parallel to the fibers ($0°$) and perpendicular to the fibers ($90°$) are always the same.
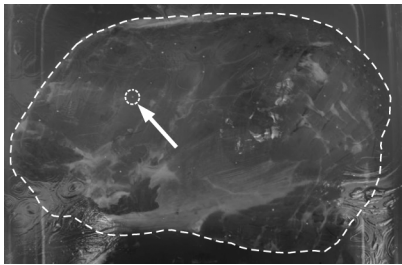

Fig. 4. Canine gluteus medius muscle sample (outlined) embedded in agar. This sample was approximately 80 mm wide and 130 mm long. Approximately 20 1-mm-diameter chrome steel bearing balls were inserted into the gel to act as point targets for registration of shear wave data to a high-resolution B-mode volume of the sample for verifying the fiber orientation. One ball is circled and shown by the tip of the arrow.

Shear wave imaging was performed on six freshly excised canine muscle samples from the thigh (semimembranosus, semitendinosus) and buttocks (gluteus medius). The samples were embedded in an agar gel with minimal acoustic attenuation and a speed of sound of approximately 1540 m/s [46], as shown in Fig. 4. The agar blocks were immersed in a water-bath during shear wave imaging to provide a standoff so that the push from the HIFU transducer could be focused in the muscle. A single acquisition was performed on each sample with the push axis approximately perpendicular to the fibers, which were visible to the naked eye. As shown in Fig. 5, this corresponds to a push axis in the two-direction, and shear wave propagation in the 1–3 plane ($\mathbf{e_1}$ and $\mathbf{e_2}$ are of course arbitrary and interchangeable). In this configuration, shear wave propagation is induced in a plane of symmetry, and can be directly viewed in a coronal plane of the 2-D matrix array image coordinates. To investigate whether it is possible to estimate the fiber orientation for the more general case when the push is not perpendicular to the fibers, four additional shear wave acquisitions on each sample were also performed with the push oblique to the fibers by tilting the 4Z1C and HIFU probe, as shown in Fig. 5. In this paper, the angle of the push relative to the fibers (θ_p, as shown in Fig. 5) will be expressed as an offset from $90°$ (i.e., $\theta_p = 0°$ for a perpendicular
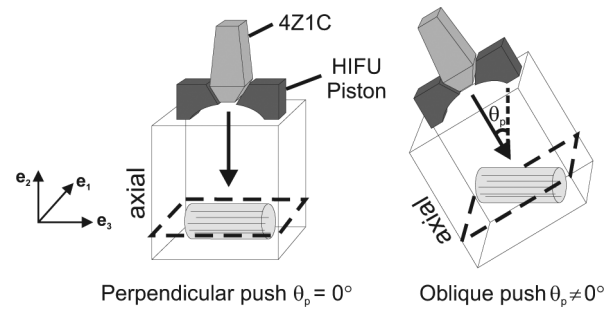

Fig. 5. Shear wave imaging setup. 4Z1C and HIFU probe were orientated so that the push axis (shown by the arrow) is perpendicular to the fibers, as shown on the left ($\theta_p = 0°$). In this configuration, shear wave propagation in a plane of symmetry can be directly observed in the coronal plane of the shear wave imaging coordinate system (shown by the dashed plane). Additional acquisitions were performed with the push oblique to the fibers by tilting the 4Z1C and HIFU probes, as shown on the right ($\theta_p \neq 0°$).

push). The maximum push tilt angle used was approximately $40°$.

B. SWS Measurement for Push Perpendicular to Fibers

As shown in Section II-A, when the push axis is perpendicular to the fibers (i.e., a push angle of $0°$), shear waves are induced in the plane perpendicular to the push. In this simplified imaging case, the coronal plane of the 2-D matrix array image coordinates directly correspond to the orientation of the plane of symmetry in which the shear wave propagates. Fig. 6(a)–(c) shows the shear wave displacement amplitude in a muscle sample at three time steps after ARFI excitation perpendicular to the fibers. Within the coronal plane at the push focus, the shape of the wave front appears elliptical, similar to the wave surface predicted by (12) and shown in Fig. 3. Indeed, the ARFI excitation from the HIFU piston is axisymmetric within this plane and can be considered a point source. Monitoring shear wave propagation in 3-D thus allows direct access to the shear wave group velocity in all directions. In addition, the shear wave phase velocity in all directions can also be estimated, as will be shown below.

In this paper, the effects of viscosity on SWS estimation in muscle are neglected as a first order approximation. The shear wave arrival-times at all locations were measured by finding the time-to-peak (TTP) of the displacement time profile [47]. Fig. 1(b) shows the shear wave arrival-time in the coronal plane at the push focus for the data-set shown in Fig. 6(a)–(c). The axial resolution of the arrival times was 0.6 mm and no averaging of the displacements or arrival-times were performed axially over the push depth-of-field. Group velocity measurement was performed by examining the arrival-time profiles within this plane along rays from the push, which is the source of the shear wave. The inverse slope of the profile gives the group velocity v_r for the corresponding ray direction ϕ_r. The group velocity was calculated for ray angles from $0°$ to $360°$ in $1°$ steps. For the wave arrival-times in Fig. 7(b), the group velocity in all directions is shown in Fig. 7(d).

As mentioned in Section II-B, the phase velocity can be measured by considering wave propagation over a small spatial region where the wavefront is approximately planar. This was done by estimating the local spatial derivative of the shear wave
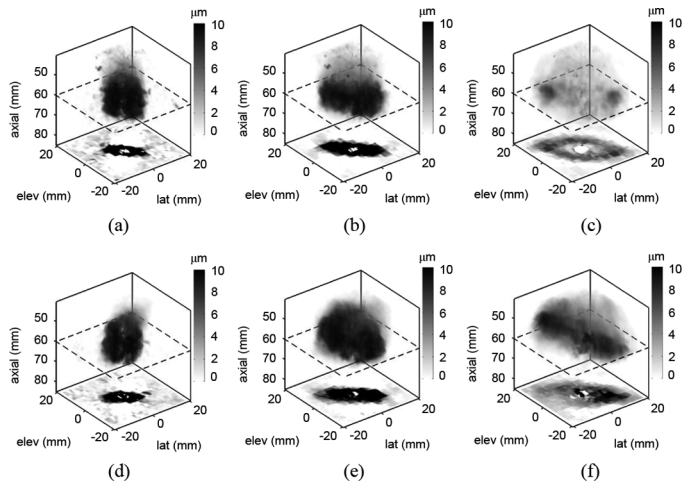
Fig. 6.   3-D displacement field in *ex vivo* muscle sample measured by the 4Z1C after ARFI excitation using the HIFU piston. The push axis was perpendicular to the fibers in the top row [(a), (c)], and oblique to the fibers in the bottom row [(d), (f)]. The displacements measured along the beamline direction using 1-D speckle tracking are shown as a volume rendering at three different time steps after the excitation. Darker voxels correspond to larger displacement amplitude. The push axis is parallel to the axial direction and is centered at the origin in the lateral and elevation dimensions. Data from the coronal plane at the push focus, outlined by the dashed lines, is projected onto the bottom of the figures. This plane corresponds to the plane of symmetry in which shear wave propagation occurs when the push is perpendicular to the fibers in (a)–(c). For this push orientation, the SWS and fiber direction can be directly estimated from data in this plane. In (d)–(f), the push is oblique to the fibers. From the perspective shown, the fibers have been rotated in the clockwise direction relative to the imaging coordinates. In this case, the tilt angle for the plane of symmetry must also be estimated. (a) Perpendicular push t = 1.6 ms. (b) Perpendicular push t = 2.9 ms. (c) Perpendicular push t = 4.5 ms. (d) Oblique push t = 1.6 ms. (e) Oblique push t = 2.9 ms. (f) Oblique push t = 4.2 ms.
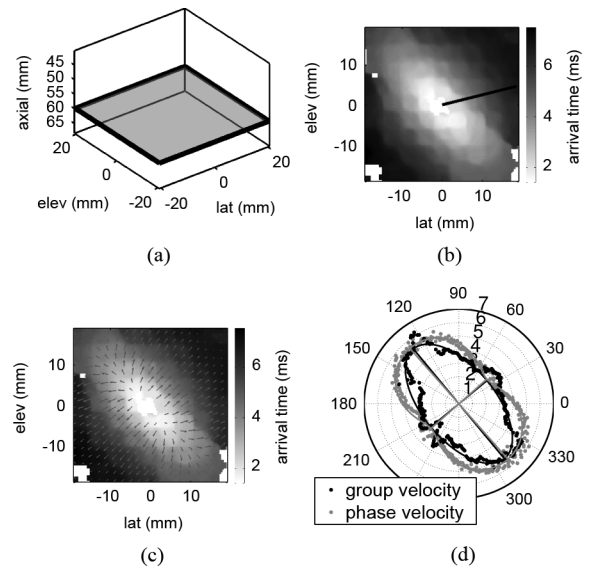

Fig. 7.   Shear wave arrival-time in the coronal plane at the push focus, as highlighted in (a), are shown in (b) and (c) for the shear wave acquisition in Fig. 6(a)–(c). Push was approximately perpendicular to the fibers so that the plane shown here corresponds to a plane of symmetry of the muscle. (b) Group velocity is calculated using the profile of arrival-times along rays from the origin, as shown for one angle ($15°$) by the black line. (c) Phase velocity can be measured from the same data by finding the local gradient of the arrival-times at all locations using finite differences. Direction and magnitude of the gradient within the coronal plane at selected points are shown by the arrows on top of the arrival-times. (d) Group velocity from (b) for all ray angles are shown in black, and the phase velocity from (c) averaged over all spatial locations in the plane as a function of phase angle in gray. Fiber orientation is estimated by fitting an ellipse to the measured group velocity or a hippopede to the phase velocity. Orientation of the major axis of the fit corresponds to the fiber direction, while the length of the major and minor axes gives the SWS along and across the fibers, respectively. Estimated SWS along the fibers from phase and group velocity measurements in this case was 5.5 m/s and 5.3 m/s, respectively, and across the fibers was 2.8 m/s and 2.7 m/s, respectively.

arrival-time. The arrival-time data was first smoothed by convolving with a 3-D Gaussian kernel with a standard deviation of 1.75 mm. The scale of this filter was chosen to suppress noise from high spatial frequencies but still provide a sufficiently localized estimate of the derivative. The spatial derivatives were then calculated at every location using finite differences. Fig. 7(c) shows the estimated gradient direction and magnitude at selected points in the coronal plane at the push focus for the data-set in Fig. 6(a)–(c). Note that the gradient vectors are 3-D and have been projected onto this plane. The average angle between the gradient vectors and the plane was 10°, and the small out-of-plane components in the axial dimension were neglected. At any location, the gradient direction corresponds to the phase angle ϕ_w, and the inverse gradient magnitude corresponds to the phase velocity v_w. The average phase velocity over all locations in the plane as a function of phase angle from 0° to 360° in 1° bins is shown in Fig. 7(d).

The fiber orientation, as well as the SWS across and along the fibers can be estimated by fitting either the shear wave phase or group velocity curves defined in (10) and (12) to the corresponding SWS measured within the plane of symmetry. Nonlinear least-squares curve fitting was performed using the Levenberg–Marquardt algorithm. Outlier speed measurements were discarded using random sample consensus (RANSAC) [48]. The phase and group velocity curves fit to the corresponding speed measurements are shown in Fig. 7(d). The fiber orientation can be estimated from the angle of the major axes of

the fitted curves, while the length of the major and minor axes give the SWS along and across the fibers, respectively. Theoretically, the fiber orientation and SWS along and across the fibers estimated from phase and group velocity measurements should be the same.

C. SWS Measurement for Push Oblique to Fibers

Fig. 6(d)–(f) shows the shear wave displacement amplitude in a muscle sample at three time steps after ARFI excitation oblique to the fibers. For this imaging scenario, shear wave propagation is still induced by the component of the push perpendicular to the fibers. However, the plane of symmetry in which shear wave propagation occurs is no longer the same orientation as the coronal plane of the image coordinates, as in Fig. 6(a)–(c).

To estimate the fiber orientation when the push is not perpendicular to the fibers, the orientation of the plane of symmetry in which shear wave propagation occurs must be found in addition to the direction of the fibers within this plane. This was done by estimating the dominant spatial orientation of the shear wave displacement amplitude using the iterative procedure shown in Fig. 8, and summarized as follows. In the first iteration, the coronal plane is used as an initial guess for a plane of symmetry. The SWS is measured in this plane as described
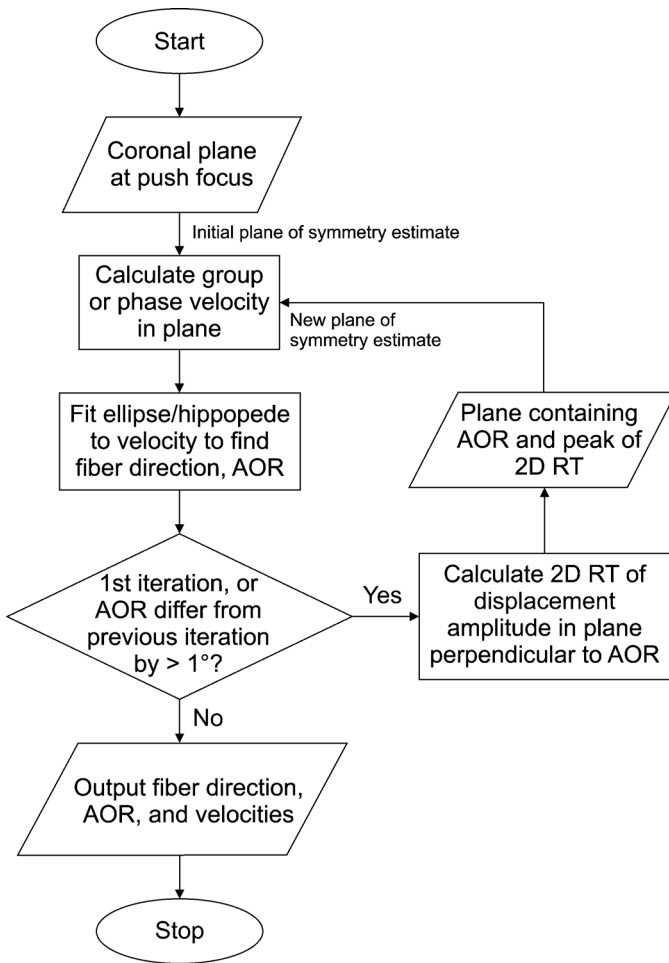
Fig. 8. Flowchart of estimating fiber orientation when push is oblique to fibers.
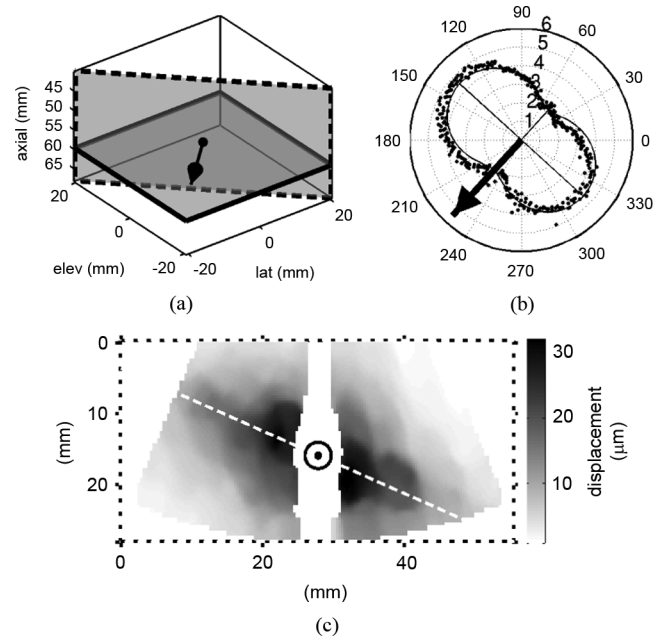

Fig. 9. Finding the plane of symmetry for an acquisition where the push was oblique to the fibers. The coronal plane at the push focus, illustrated by the plane with the solid outline in (a), is used as an initial guess for a plane of symmetry. (b) Phase velocity measured in the coronal plane. Direction perpendicular to the fibers can be estimated by fitting a hippopede to the phase velocity in this plane and finding its minor axis, which is shown by the arrow in (a) and (b). This direction corresponds to the axis of rotation (AOR) for the tilt between the push and the fibers. Alternatively, the AOR can be estimated from group velocity measurements and fitting an ellipse. (c) Shear wave displacement amplitude in the plane orthogonal to the AOR. The orientation of this plane is shown in (a) by the dashed lines. AOR [arrow in (a) and (b)] points out of the page in (c) and is shown by the circled dot. White dashed line shows the fiber direction estimated by finding the dominant orientation of the displacement amplitude in this plane using the 2-D radon transform (2-D RT). The plane passing through this line and the AOR gives an updated estimate for the plane of symmetry. SWS and the AOR is recalculated using data in this plane and another iteration is performed if the AOR differs by more than $1°$. Algorithm converged in two iterations for this example and the estimated tilt angle was $19.9°$, whereas the true angle measured from the separate high-resolution B-mode validation experiment was $19.5°$.

in the previous subsection using either the group or phase velocity. The angle of the 3-D phase velocity vectors out of the coronal plane for oblique pushes were larger than for the perpendicular push cases, but was still on average below $25°$ over the entire coronal plane in all data-sets. Thus, sampling the arrival-times in the coronal plane still allows an approximation of the true SWS to be calculated. Next, the direction perpendicular to the fibers (the direction with the smallest speed) is estimated by fitting an ellipse or hippopede to the measured speeds in the coronal plane, as shown in Fig. 9(b). This direction is invariant under a rotation between the push and the fibers and corresponds to the axis of rotation (AOR) for the tilt angle. Then, the shear wave displacement amplitude at spatial locations in the plane perpendicular to this axis is found, as shown in Fig. 9(c). The displacement amplitude was measured using the maximum displacement 2–9.6 ms after ARFI excitation to avoid the initial high amplitude displacements within the region of excitation (ROE) not associated with shear wave propagation. The 2-D radon transform (2-D RT) of this data is then computed. The peak of the 2-D RT is used to find the line which maximizes the sum of the displacement amplitude along its length, as shown in Fig. 9(c). The orientation of this line gives an updated estimate of the fiber direction, and the plane passing through the line and the AOR gives an new estimate for the plane of symmetry. This plane is then used as the input in another iteration

of the algorithm to further refine the fiber orientation estimate. Each iteration generates a new estimate for the plane of symmetry using the AOR from the previous iteration, and the AOR is updated using the SWS in the new plane. The algorithm terminates when the change in angle between the AOR estimated in successive iterations is less than $1°$. The SWS and principle axes computed from the plane of symmetry in the final iteration is returned.

D. Fiber Orientation From B-mode

To independently verify the muscle fiber orientation estimated from shear wave imaging, B-mode ultrasound volumes of the samples were used to measure fiber orientation. Individual fasciculi can be identified on B-mode as hypoechoic cylindrical structures, surrounded by thin, linear hyperechoic connective tissue called the perimysium [27]. Unfortunately, due to the low frequency of the 4Z1C matrix array (2.8 MHz), these structures were not clearly apparent in the B-mode volumes acquired during shear wave imaging. Therefore, the muscle samples were scanned using a 14MHz 1-D array (14L5 on the S2000 scanner, Siemens Healthcare, Ultrasound
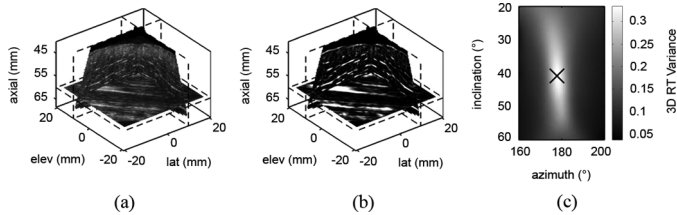
Fig. 10. (a) High-resolution 14L5 B-mode volume of a muscle sample used to measure fiber orientation. (b) B-mode volume in (a) after line enhancement filtering. (c) Variance of the 3-D RT of the line enhanced B-mode in (b) for various 3-D orientations. The maximum variance (marked by cross) corresponds to the dominant fiber orientation.

Business Unit, Mountain View, CA, USA). The 14L5 was mechanically swept over the samples using a translation stage (Model MM3000, Newport Corporation, Irvine, CA, USA) in 0.1 mm steps to obtain high-resolution 3-D B-mode volumes of the samples, an example of which is shown in Fig. 10(a).

To register the 14L5 volumes to the 4Z1C shear wave imaging coordinates, the location of 1-mm-diameter chrome steel bearing balls embedded in the agar surrounding the muscle were identified in the 14L5 and 4Z1C B-mode images. These balls can be seen in Fig. 4, and appear in B-mode as point targets, as shown in Fig. 11. Their locations were determined by manually identifying the region of interest surrounding the target, thresholding, and calculating the image centroid. The 14L5 and 4Z1C volumes were rigidly registered by minimizing the square of the distance between the corresponding point target locations [49], as shown in Fig. 11(c). Approximately 20 balls were used as targets for registration for each sample, and the root mean square (rms) target registration error was typically under 2 mm.

Automatic measurement of muscle fiber orientation in 2-D B-mode images has previously been performed using the radon transform [50], [51]. In this study, the approach used by Rana *et al.* [50] was extended to 3-D. To enhance the linear structure of the perimysium surrounding the fasciculi and suppress speckle noise, the 3-D multiscale vessel enhancement filter described by Frangi *et al.* [52] was applied to the 14L5 B-mode. First, the image was convolved with 3-D Gaussian kernels with standard deviations of 0.1, 0.3, and 0.5 mm to provide smoothing at different scales. The eigenvalues of the 3-D Hessian matrix of the smoothed images, which provides information on the shape of curvature changes in the image, were then analyzed using the vesselness function defined in [52]. The thresholds $\alpha = 0$, $\beta = 0.5$, and $c = 0.75$ were used in the vesselness function to maximize the filter response for the hyperechoic perimysium. This was repeated at every voxel for the three different scales, and the maximum response across the different scales was used as the filter output. The B-mode volume in Fig. 10(a) after filtering is shown in Fig. 10(b).

To determine the predominant orientation of the fibers, the 3-D Radon Transform (3-D RT) of the 14L5 B-mode after line enhancement filtering was computed for all possible 3-D orientations. For each orientation, the 3-D RT is computed by projecting a 2-D grid of parallel rays from that angle onto the volume. The integral of the volume voxels along each ray is recorded. The output of the 3-D RT for that orientation is the 2-D image formed by all the rays in the grid. The 3-D RT was calculated for spherical angles of $0° \leq \theta \leq 90°$ (inclination), and $0° \leq \phi \leq 360°$ (azimuth), which constitutes a hemisphere. Note that angles on only one half of a sphere need to be considered since view-points on opposite sides (antipodes) give the same 3-D RT. When the 3-D RT orientation matches the predominant fiber angle, the output image will have high values where the rays are coincident to the hyperechoic perimysium, and low values where they pass through the hypoechoic fasciculi. In contrast, when the 3-D RT orientation is not aligned with the fibers, all the rays will tend to pass through equal numbers of bright and dark voxels, giving a more uniform output image. Thus, the dominant fiber orientation can be determined by searching for the angle where the 3-D RT has the greatest variance. The peak 3-D RT variance for the volume in Fig. 10(b) is shown in Fig. 10(c).

IV. RESULTS

A. Fiber Angle for Push Perpendicular to Fibers

The registered 14L5 B-mode and 4Z1C shear wave data for one acquisition when the push was perpendicular to the fibers is shown in Fig. 12(b). The phase and group velocities measured in the coronal plane are shown in Fig. 12(c), along with the true fiber orientation measured by 3-D RT, which is projected onto the plane. The errors in the fiber orientation estimated using phase and group velocity measurements were $1.6°$ and $1.9°$, respectively. Note that some of this error includes the angle between the true fiber orientation measured using 3-D RT, and the image coronal plane, which was assumed to be a plane of symmetry in alignment with the fibers in the SWS experiment. This angle would be zero if the push was oriented perfectly perpendicular to the fibers in the SWS experimental setup. In this case, a slight tilt of $1.5°$ existed. The average error in the fiber orientation estimated using phase and group velocity when the push was oriented approximately perpendicular to the fibers for the six samples (total of six acquisitions) was $3.5 \pm 2.6°$ and $3.4 \pm 1.4°$ (mean ± standard deviation), respectively. The average tilt angle for the push due to misalignment in the setup procedure was $2.5 \pm 2.0°$ over the six acquisitions.

B. Fiber Angle for Push Oblique to Fibers

The registered 14L5 B-mode and 4Z1C shear wave data for one acquisition when the push was oblique to the fibers is shown in Fig. 13(b). The tilt angle for the plane of symmetry estimated using the displacement amplitude as described in Section III-C was $19.9°$. In comparison, the true tilt angle measured by 3-D RT was $19.5°$. The error in the 3-D fiber orientation from phase and group velocity measurements in the estimated plane of symmetry was $0.5°$ and $2.1°$, respectively, for this case. Note that this overall error includes both inaccuracies in estimating the tilt angle (orientation of the plane of symmetry) using the displacement amplitude, as well as the fiber orientation within the plane of symmetry using the SWS.

The plane of symmetry orientation estimated for 30 acquisitions taken with a variety of push angles on the six samples is shown in Fig. 14(a) versus the true angle measured by 3-D RT. The average error in the estimated push angle was $3.3 \pm 2.4°$.
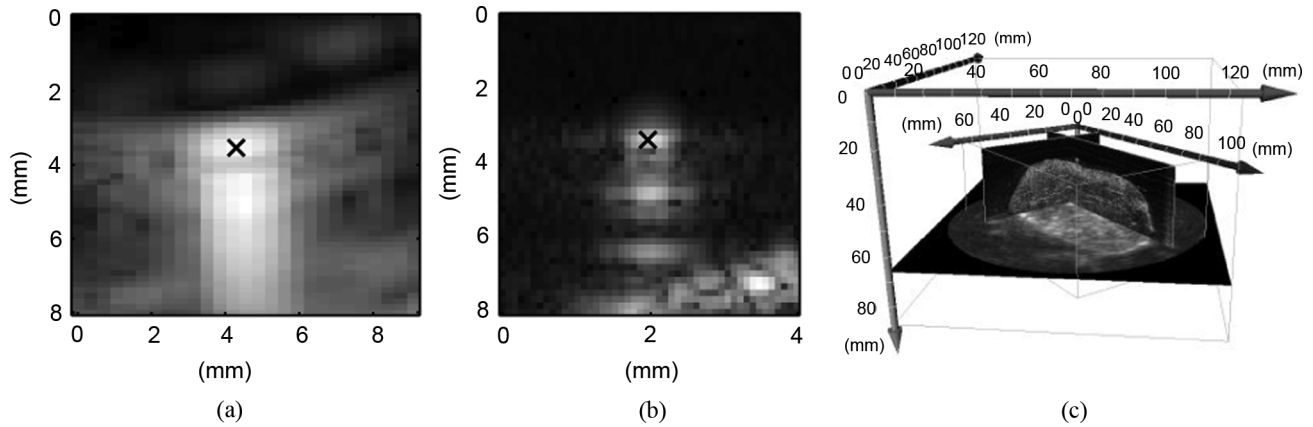
Fig. 11. (a) Bearing ball in 4Z1C B-mode, with its centroid location marked by a cross. (b) Bearing ball in 14L5 B-mode, with its centroid location marked by a cross. (c) Registered 4Z1C and 14L5 B-mode volumes. Nineteen bearing balls were used as fiducial markers for registration in this example, and the rms target registration error was 1.9 mm.

Fig. 13. High-resolution 14L5 B-mode registered to 4Z1C shear wave data for an acquisition where the push was oblique to the fibers. (a) Data from the plane orthogonal to the axis of rotation (AOR) estimated using the procedure in Fig. 8 is shown. (b) Shear wave displacement amplitude at one time step is overlaid on top of the 14L5 B-mode in this plane. Plane of symmetry angle estimated from the displacement amplitude is shown by the dashed line. True angle determined from the high-resolution 14L5 B-mode using the 3-D RT is shown by the arrows. Difference between the two was 0.4° in this case. Fiber orientation was determined from the phase and group velocity measurements in the estimated plane of symmetry. Error in the 3-D fiber orientation was 0.5° from phase velocity and 2.1° from group velocity measurements for this example.
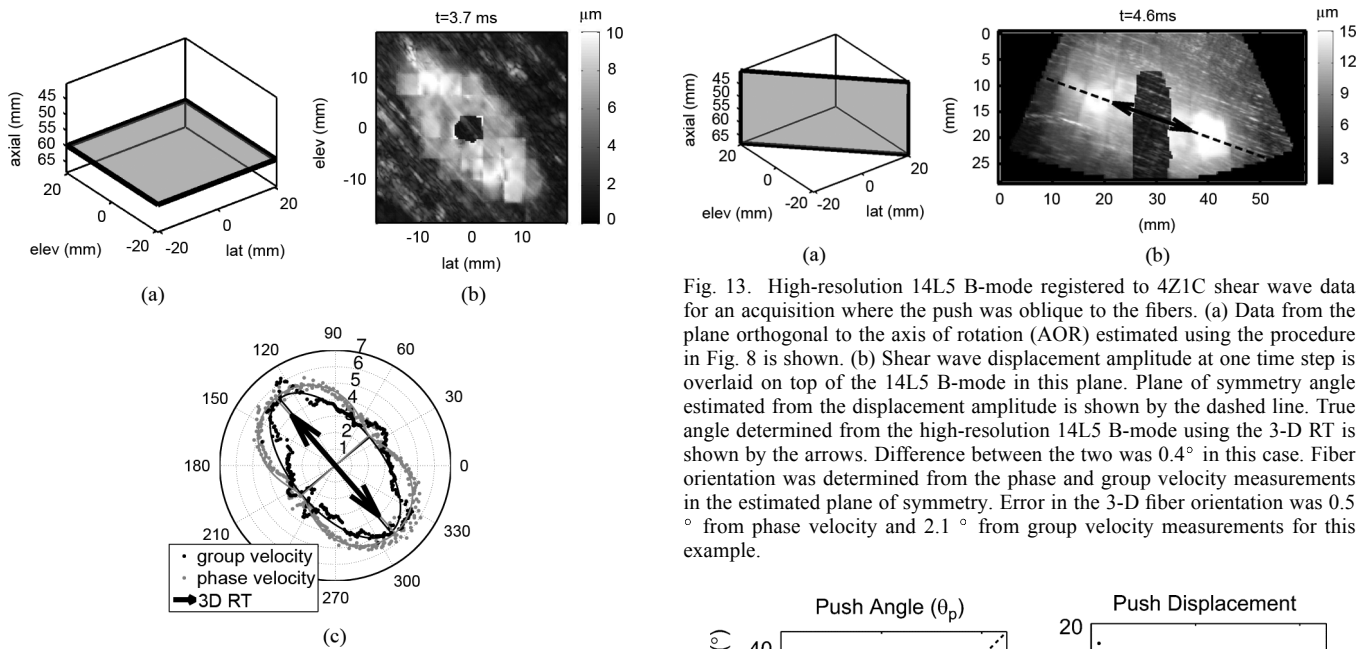

Fig. 12. High-resolution 14L5 B-mode registered to 4Z1C shear wave data for an acquisition where the push was perpendicular to the fibers. (a) Data from the coronal plane at the push focus is shown. (b) Shear wave displacement amplitude at one time step is overlaid on top of the 14L5 B-mode in this plane. (c) Group and phase velocity of the shear wave in (b) in the coronal plane and the fitted ellipse and hippopede. The fiber orientation is estimated from the major axes of the fitted curves. True fiber orientation determined from the 14L5 B-mode using the 3-D RT is shown by the arrows. Error in the fiber orientation estimated from phase and group velocities in this case was 1.6° and 1.9°, respectively.

Fig. 14(b) shows the displacement amplitude at the push focus as a function of push angle. The median peak displacement within 5 mm of the push axis and inside the focal depth-of-field (54–66 mm axially) was used to measure the push displacement amplitude. The overall 3-D error in the fiber orientation determined from phase and group velocity measurements in estimated plane of symmetry for the 30 acquisitions was $5.4 \pm 2.9°$ and $5.3 \pm 3.2°$, respectively.

C. Shear Wave Speed

The mean and standard deviation of the estimated SWS along and across the fibers obtained from five different push angles

Fig. 14. (a) Estimated push angle (y-axis) for 30 acquisitions on the six muscle samples versus the true angle (x-axis). Dashed line indicates a slope of unity. Plane of symmetry orientation was estimated using the procedure shown in Fig. 8, and the true angle was measured from the high-resolution 14L5 B-mode using the 3-D RT. Mean error was $3.5 \pm 2.8°$. (b) Median peak displacement in time within 5 mm of the push axis inside the push depth-of-field (54–66 mm) as a function of push angle. Coefficient of determination (r^2) between the two variables is 0.43.

(approximately 0°, 10°, 20°, 30°, and 40°) on each of the six samples are shown in Fig. 15. An outlier case for the phase velocity measurement along the fibers occurred for a push angle of 35° on sample 1. This acquisition had a push displacement

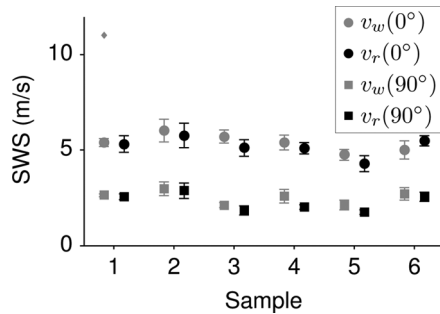Fig. 15. Phase velocity (v_w) and group velocity (v_r) along ($0°$) and across ($90°$) the fibers averaged over the five push angles used for each sample (including the case when the push was perpendicular to the fibers). The diamond indicates an outlier phase velocity measured for a push angle of $35°$ on sample 1.

amplitude of $3.5\ \mu m$, which was the lowest of the 30 acquisitions [see Fig. 14(b)]. While the estimated phase velocity along the fibers was incorrectly high for this case, the estimated phase velocity across the fibers, and group velocities for both propagation directions, were still consistent with those obtained using other push angles on this sample. In addition, the fiber direction was also correctly estimated (the error was $5.1°$) from the phase velocity measurements in this case.

V. DISCUSSION

Shear wave propagation induced by focused ARFI excitation can be monitored in 3-D using a 2-D matrix array transducer by electronically steering the tracking beam in both the lateral and elevation directions. In contrast, with conventional 1-D arrays, shear wave propagation can only be monitored in one plane unless the probe is physically repositioned, which limits the number of directions the SWS can be practically measured to assess anisotropy. Since a maximum of 64 parallel receive channels on the SC2000 scanner was available, 81 repeated ARFI excitations were required to monitor shear wave propagation at all the beam locations in the FOV used in this study. The number of repeat ARFI excitations could be reduced with more parallel receive channels or single channel data acquisition and software beamforming. Alternatively, the number of tracking locations could be reduced at the expense of spatial resolution, or different tracking locations could be interrogated in turn temporally at the expense of temporal resolution. The minimum time interval between repeated ARFI excitations using the HIFU piston is only physically limited by the shear wave tracking duration, which was 16 ms in this study. If the 81 pushes used to acquire data could be repeated at this rate, the total acquisition time would only be 1.3 s. Unfortunately, due to current software limitations for saving data on the SC2000, a lengthy delay of 22 s was necessary between excitations. If data transfer on the SC2000 could be made more efficient, then the long acquisition time of 30 min currently required could be reduced significantly.

One of the challenging aspects of performing shear wave imaging in skeletal muscle using conventional 1-D array ultrasound transducers is that the orientation of the transducer relative to the fibers is usually not known precisely. Visualization of muscle fibers in B-mode requires the use of a high frequency transducer, which is not always available. In addition, determi-

nation of the fiber orientation, which is 3-D in nature, from 2-D cross-sectional images is not a trivial task. Indeed, measurement of the true fiber orientation required scanning the muscle samples using a high frequency ultrasound transducer mounted on a translation stage in a separate experiment in this study. Due to the anisotropic SWS in muscle, misregistration of the imaging plane and the fibers can introduce error in the measurement of SWS along and across the fibers for quantification of the longitudinal and transverse shear moduli. A major advantage of monitoring shear wave propagation in 3-D using a 2-D matrix array is that both the phase and group velocity in all directions can be measured in a plane of symmetry of the muscle, as shown in Fig. 7. This study has demonstrated that by fitting the theoretical relationship for SWS in a TI material [shown in (10) and (12)] to the measured speeds in different directions, the true fiber orientation can be estimated. This eliminates the need for knowledge of the fiber direction during imaging and enables the SWS along and across the fibers to be measured independent of the probe orientation.

The most straightforward imaging scenario for measuring SWS anisotropy in skeletal muscle using a 2-D matrix array is to orient the push axis perpendicular to the fibers. As shown in Fig. 6(a)–(c), this induces a shear wave in the image coronal plane, which is also a plane of symmetry of the muscle. The shear wave phase and group velocity in all directions relative to the fiber can therefore be measured using the shear wave data within this plane. In this study, the push axis was able to be oriented approximately perpendicular to the fibers by visual inspection, as the fibers of the *ex vivo* muscle samples ran parallel to their surface and were visible to the naked eye. For the six samples imaged, a fairly accurate alignment of the push axis was achieved using this procedure, with an average tilt angle of $2.5 \pm 2.0°$.

In *in vivo* shear wave imaging scenarios, perpendicular alignment of the push axis to the fibers may be more difficult. First, the muscle plane of symmetry would not be visible to the naked eye as for the *ex vivo* samples. In addition, as mentioned previously, fiber orientation may not be visible in B-mode either if low frequency transducers are used for shear wave imaging. Finally, the acoustic window available for imaging *in vivo* may limit the physical orientation of the transducer. Therefore, in this study, data was also acquired on all the samples for the more general imaging case when the push is oblique to the fibers. It can be seen on Fig. 6(d)–(f) that in this configuration, shear wave propagation is still induced, but its plane of propagation occurs at an angle to the image coronal plane. The dominant direction of shear wave propagation can be found using the procedure shown in Fig. 8. This angle is shown to correspond to the plane of symmetry orientation (tilt between the push and the fibers) in Fig. 13(b) and Fig. 14(a). By calculating the phase and group velocity in the plane of symmetry determined using this procedure, the SWS along and across the fibers, and the fiber orientation can be estimated when the push is oblique to the fibers. The mean error in estimating the plane of symmetry for 30 acquisitions with various push angles up to approximately $40°$ was $3.3 \pm 2.4°$. This is only slightly larger than the error in alignment when attempting to position the push axis perpendicular to the fibers during imaging, which was $2.5 \pm 2.0°$. The

overall 3-D fiber orientation error after estimating the angle of the plane of symmetry for the 30 acquisitions was $5.4 \pm 2.9°$ for phase velocity measurements, and $5.3 \pm 3.2°$ for group velocity measurements. This was slightly larger than the 3-D fiber orientation errors of $3.5 \pm 2.6°$ and $3.4 \pm 1.4°$ from phase and group velocity measurements for the six acquisitions when the push was perpendicular to the fibers and the image coronal plane could be assumed to be a plane of symmetry. As mentioned above, the error when attempting to align the push axis perpendicular to muscle fibers is likely to be greater *in vivo*, so the additional error associated with estimating the plane of symmetry orientation is not likely to be significant in practice.

Consistent values of SWS along and across the fibers were measured with different push angles, as shown by the error bar sizes in Fig. 15. This suggests that SWS measurements can be made independent of the push angle. However, as Fig. 14(b) shows, the displacement amplitude at the push focus decreases as the push axis is tilted towards the fiber direction. This causes the shear wave amplitude to decrease for larger tilt angles, and makes accurate SWS measurements more challenging in these cases. Indeed, one outlier phase velocity measurement along the fibers occurred for a highly oblique push angle of 35° on Sample 1, shown by the diamond in Fig. 15. This acquisition had the lowest displacement amplitude at the push focus of all the data-sets. Although the phase velocity along the fibers were incorrectly measured, the velocity across the fibers and the fiber direction were still estimated correctly from the phase velocity measurements for this case.

The decrease in ARFI displacement amplitude as the push is tilted towards the fiber direction can be explained by two directionally dependent factors. One is anisotropic acoustic scattering properties in muscle. It has previously been shown that the acoustic attenuation coefficient of skeletal muscle is a factor of 2 greater at 45° to the fibers than perpendicular to the fibers [53]. A higher acoustic attenuation leads to greater loss of energy in the near-field of the pushing beam, smaller radiation force amplitudes within the depth-of-field, and thus smaller displacement amplitudes at the focus [54]. The other factor is the anisotropic mechanical properties of muscle. Since the shear modulus is greater along the fibers than across, the effective stiffness in the push direction increases as the push angle varies from perpendicular to parallel to the fibers. Both of these factors contribute to the decrease in displacement amplitude near the excitation focus as the tilt angle of the push increases.

The ratio between the SWS along and across the fibers in all the samples was approximately 2:1, which is in agreement with the degree of anisotropy observed in skeletal muscle in other studies [10], [20], [21]. The range of SWS observed in this study is also consistent with that reported elsewhere [10], [21], [28]. Nevertheless, caution must be used in comparing absolute speed measurements in different studies due to the wide range of conditions under which imaging has been performed on muscle, whose stiffness is dynamic and can vary over two orders of magnitude [20]. In this study, *ex vivo* muscle samples embedded in agar were imaged. Although the SWS measured herein may not be representative of realistic values *in vivo*, fixing the muscles rigidly in agar enabled the true 3-D fiber orientation of the samples to be verified in this study.

The fiber orientation and SWS along and across the fibers obtained with phase and group velocity measurements were comparable. Additional smoothing of the arrival-times was performed spatially in order to calculate the phase velocity, and this is probably the cause of the smoother appearance of the phase velocity profile compared to the group velocity shown in Fig. 7(d). However, as shown in the same figure, differences in the estimated SWS along and across the fibers from both sets of velocity measurements are small once the theoretical velocity curves are fit to the experimental data to provide additional smoothing.

The group velocity is perhaps the most intuitive measure of speed, and its relationship with direction has a clear physical interpretation as the wave surface. Group velocity measurement (along a ray from the source to an observer) is the approach usually taken to estimate the SWS in ultrasound based radiation force shear wave imaging methods. This is largely due to the fact that using conventional 1-D arrays for monitoring shear wave propagation only allows measurement of the SWS along a single ray from the radiation force excitation. By using a 2-D matrix array to track shear wave propagation in 3-D in this study, the local phase velocity at every spatial location was able to be measured. Phase velocity measurement has several advantages over group velocity in the context of anisotropy. Mathematically, phase velocity is a more tractable concept than group velocity. Expressions for phase velocity can be easily derived from Christoffel's equation, as shown in Section II-A. The group velocity, on the other hand, must be found parametrically from the phase velocity using the transformation in (11). In the case of shear waves in TI media, an analytical expression exists for the group velocity (12), but an analytical expression may not exist for other wave-modes. In addition, the phase velocity is always a single valued function of direction, whereas the group velocity can take on multiple values. Measurement of group velocity also relies on having a point source at a known location. In this study, the location of the push focus from the HIFU piston was known to be at the center of the FOV of the imaging array [44]. In addition, the focal geometry of the HIFU piston is axisymmetric and is a good approximation for a point source. When the location of the source is not known precisely, or the focus of the ARFI excitation is not axisymmetric, bias in group velocity measurements can occur [55]. In these situations, phase velocity measurements, which do not require the location or timing of the source to be known *a priori*, may provide a more accurate measurement of the SWS.

The effects of dispersion due to viscosity were neglected in this study as a first-order approximation. However, it has been reported that shear waves propagating in muscle is subject to appreciable dispersion due to viscosity [10], [20], [37], [43]. In particular, Deffieux *et al.* and Gennisson *et al.* showed that the viscoelastic properties of muscle were anisotropic, with greater dispersion across the fibers than along the fibers [20], [43]. Dispersion due to viscosity could also be analyzed using the data from the 2-D matrix array in this study, since a broadband excitation was used to induce shear waves. To analyze the effects of viscosity, the Fourier shear wave spectroscopy technique described by Deffieux *et al.* [43] could be applied. This method uses phase information of the Fourier transform to find

the arrival-times of individual shear wave frequency components. It would be relatively straightforward to substitute the arrival-times measured using the TTP in this study with the phase information from Fourier analysis to account for the effects of both anisotropy and viscosity on the SWS. This would allow the SWS to be characterized both as a function of frequency and direction. Such analysis was outside the scope of this paper, but will be investigated in future studies. Shear wave imaging using a 2-D matrix array could thus potentially be a valuable tool to assess viscoelastic anisotropy in tissue.

In this study, only shear wave propagation was observed in muscle when the push was oblique to the fibers. However, it should be theoretically possible to also generate the quasi-shear wave-mode, which was described in Section II-A. In particular, the wave propagating in the coronal plane should be a superposition of shear and quasi-shear wave modes for an oblique push. However, no evidence of any change in the wavefront shape in this plane was observed when the push axis was tilted. As shown in Fig. 6(d)–(f), the wavefront still appears elliptical for an oblique push, and the velocity measurements in this plane still fits the theoretical relationship for a shear wave, as shown in Fig. 9(b). It is possible that the wave amplitude is dominated by the shear wave mode, or that the difference between shear and quasi-shear wave speeds is too subtle to allow clear separation of the two wave modes within extent of the imaging FOV. If the quasi-shear wave speed could be quantified, it would allow the ratio between the Young's moduli along and across the fibers for a TI material in the limit of incompressibility to be determined [21]. This parameter, along with the shear moduli along and across the fibers, would allow an incompressible TI material to be completely characterized.

Another interesting finding of this study is that when the push is oblique to the fibers, the dominant direction of wave propagation occurs along the fibers, as shown in Fig. 13(b). This effect was used to find the push angle in Section III-C. The wave amplitude at an angle to the fibers is significantly smaller, which cannot be explained by transverse isotropy alone. Some other effect, such as the fibers acting as wave guides or directional dependent shear wave attenuation due to viscoelastic anisotropy are possible explanations, and should be investigated in future work.

The muscle samples imaged in this study were approximately homogeneous and their fiber directions were uniform within the imaging FOV. Hence, TI, which is the simplest model of anisotropy, could be used to model their behavior. Shear wave data within a single plane of symmetry is sufficient for characterizing the anisotropic SWS in this case. Future studies with the 2-D matrix array could be performed in media with more complicated structure, such as the myocardium, which is known to have layers of fibers in different orientations [18]. In this case, SWS anisotropy would vary as a function of depth and require data in multiple planes to be analyzed.

One disadvantage of using the HIFU transducer for ARFI excitation in this study is that it has a fixed focus at only one location, resulting in a limited depth-of-field of 12 mm over which the shear wave can be approximated as planar. Due to the high cost of the transducer and potential for damage to the electronics within the probe handle at ARFI intensities, ARFI excitation

using the 4Z1C 2-D matrix has not yet been attempted in our lab. However, this could be an option in the future with continued improvements in transducer technology. Having the capability to spatially modulate the acoustic radiation force excitation in 3-D using a 2-D matrix array would open new possibilities in shear wave imaging. For example, a supersonic excitation [9] could be implemented to extend the excitation depth-of-field, which could potentially be advantageous in mapping 3-D fiber orientations that varies with depth.

The separate HIFU transducer used for ARFI excitation in this study is suitable for long duration high intensity ultrasound excitations, unlike conventional diagnostic transducers. Therefore, this system could be used to investigate 3-D shear wave imaging using harmonic shear wave excitations similar to the SDUV method described by Chen *et al.* [10]. This would allow the frequency of the shear wave used for imaging to be precisely controlled. In addition, the combined 4Z1C/HIFU system could potentially be used to study monitoring of therapeutic procedures performed by the HIFU transducer.

VI. CONCLUSION

Using a 2-D matrix array transducer to monitor ARFI induced shear wave propagation in 3-D, the 3-D muscle fiber orientation, as well as the SWS along and across the fibers can be estimated from a single shear wave acquisition. Moreover, these measurements can be performed independent of transducer orientation with respect to the fibers. Both the phase and group velocity can be measured from 3-D shear wave data, and either velocity can be used to estimate the fiber direction and SWS along and across the fibers with comparable results. When the ARFI push axis can be oriented perpendicular to the fibers, shear wave data within the image coronal plane can be used to measure SWS and fiber orientation. The average 3-D fiber orientation error measured by phase and group velocities in six muscle samples when the push was approximately perpendicular to the fibers were $3.5 \pm 2.6°$ and $3.4 \pm 1.4°$, respectively. For the more general imaging case when the push is oblique to the fibers, the angle between the push and the fibers can be estimated by finding the direction along which shear wave amplitude is the largest. For 30 acquisitions in the six muscle samples with oblique push angles of up to 40°, mean errors in the measured 3-D fiber orientation were $5.4 \pm 2.9°$ and $5.3 \pm 3.2°$ from phase and group velocity measurements respectively, after estimating the push angle. Although the 3-D fiber orientation can be estimated when the push is not perpendicular to the fibers, the ARFI induced shear wave displacement amplitude decreases as the push is tilted towards the fibers. For this reason, outlier estimates of the SWS can occur for highly oblique push angles.

REFERENCES

[1] H. Kanai, "Propagation of spontaneously actuated pulsive vibration in human heart wall and in vivo viscoelasticity estimation," *IEEE Trans. Ultrason., Ferroelectr., Freq. Control*, vol. 52, no. 11, pp. 1931–1942, Nov. 2005.

[2] M. Couade, M. Pernot, C. Prada, E. Messas, J. Emmerich, P. Bruneval, A. Criton, M. Fink, and M. Tanter, "Quantitative assessment of arterial wall biomechanical properties using shear wave imaging," *Ultrasound Med. Biol.*, vol. 36, no. 10, pp. 1662–1676, 2010.

[3] T. Gallot, S. Catheline, P. Roux, J. Brum, N. Benech, and C. Negreira, "Passive elastography: Shear-wave tomography from physiological-noise correlation in soft tissues," *IEEE Trans. Ultrason., Ferroelectr., Freq. Control*, vol. 58, no. 6, pp. 1122–1126, Jun. 2011.

[4] K. Sabra, S. Conti, P. Roux, and W. Kuperman, "Passive in vivo elastography from skeletal muscle noise," *Appl. Phys. Lett.*, vol. 90, no. 19, pp. 194 101–194 101, 2007.

[5] M. Yin, J. A. Talwalkar, K. J. Glaser, A. Manduca, R. C. Grimm, P. J. Rossman, J. L. Fidler, and R. L. Ehman, "Assessment of hepatic fibrosis with magnetic resonance elastography," *Clin. Gastroenterol. Hepatol.*, vol. 5, no. 10, pp. 1207–1213, 2007.

[6] L. Huwart, F. Peeters, R. Sinkus, L. Annet, N. Salameh, L. C. t. Beek, Y. Horsmans, and B. E. V. Beers, "Liver fibrosis: Non-invasive assessment with MR elastography," *NMR Biomed.*, vol. 19, pp. 173–179, 2006.

[7] L. Sandrin, B. Fourquet, J.-M. Hasquenoph, S. Yon, C. Fournier, F. Mal, C. Christidis, M. Ziol, B. Poulet, F. Kazemi, M. Beaugrand, and R. Palau, "Transient elastography: A new noninvasive method for assessment of hepatic fibrosis," *Ultrasound Med. Biol.*, vol. 29, no. 12, pp. 1705–1713, 2003.

[8] A. P. Sarvazyan, O. V. Rudenko, S. D. Swanson, J. B. Fowlkes, and S. Y. Emelianov, "Shear wave elasticity imaging: A new ultrasonic technology of medical diagnostics," *Ultrasound Med. Biol.*, vol. 24, no. 9, pp. 1419–1435, 1998.

[9] J. Bercoff, M. Tanter, and M. Fink, "Supersonic shear imaging: A new technique for soft tissue elasticity mapping," *IEEE Trans. Ultrason., Ferroelectr., Freq. Control*, vol. 51, no. 4, pp. 396–409, Apr. 2004.

[10] S. Chen, M. Urban, C. Pislaru, R. Kinnick, Y. Zheng, A. Yao, and J. Greenleaf, "Shearwave dispersion ultrasound vibrometry (SDUV) for measuring tissue elasticity and viscosity," *IEEE Trans. Ultrason., Ferroelectr., Freq. Control*, vol. 56, no. 1, pp. 55–62, Jan. 2009.

[11] K. Nightingale, S. McAleavey, and G. Trahey, "Shear-wave generation using acoustic radiation force: In vivo and ex vivo results," *Ultrasound Med. Biol.*, vol. 29, no. 12, pp. 1715–1723, 2003.

[12] R. Muthupillai, D. Lomas, P. Rossman, J. Greenleaf, A. Manduca, and R. Ehman, "Magnetic resonance elastography by direct visualization of propagating acoustic strain waves," *Science*, vol. 269, no. 5232, pp. 1854–1857, 1995.

[13] M. Palmeri, M. Wang, N. Rouze, M. Abdelmalek, C. Guy, B. Moser, A. Diehl, and K. Nightingale, "Noninvasive evaluation of hepatic fibrosis using acoustic radiation force-based shear stiffness in patients with nonalcoholic fatty liver disease," *J. Hepatol.*, vol. 55, no. 3, pp. 666–672, 2011.

[14] É. Bavu *et al.*, "Noninvasive in vivo liver fibrosis evaluation using supersonic shear imaging: A clinical study on 113 hepatitis c virus patients," *Ultrasound Med. Biol.*, vol. 37, no. 9, pp. 1361–1373, 2011.

[15] L. Huwart, C. Sempoux, E. Vicaut, N. Salameh, L. Annet, E. Danse, F. Peeters, L. C. t. Beek, S. R. Rahier, J.Y Horsmans, and B. E. V. Beers, "Magnetic resonance elastography for the noninvasive staging of liver fibrosis," *Gastroenterology*, vol. 135, no. 1, pp. 32–40, 2008.

[16] R. Sinkus, M. Tanter, T. Xydeas, S. Catheline, J. Bercoff, and M. Fink, "Viscoelastic shear properties of in vivo breast lesions measured by MR elastography," *Magn. Reson. Imag.*, vol. 23, no. 2, pp. 159–165, 2005.

[17] M. Tanter, J. Bercoff, A. Athanasiou, T. Deffieux, J. L. Gennisson, G. Montaldo, M. Muller, A. Tardivon, and M. Fink, "Quantitative assessment of breast lesion viscoelasticity: Initial clinical results using supersonic shear imaging," *Ultrasound Med. Biol.*, vol. 34, no. 9, pp. 1373–1386, 2008.

[18] W. Lee, M. Pernot, M. Couade, E. Messas, P. Bruneval, A. Bel, A. Hagege, M. Fink, and M. Tanter, "Mapping myocardial fiber orientation using echocardiography-based shear wave imaging," *IEEE Trans. Med. Imag.*, vol. 31, no. 3, pp. 554–562, Mar. 2012.

[19] R. Bouchard, S. Hsu, P. Wolf, and G. Trahey, "In vivo cardiac, acoustic-radiation-force-driven, shear wave velocimetry," *Ultrason. Imag.*, vol. 31, no. 4, pp. 201–213, 2009.

[20] J. Gennisson, T. Deffieux, E. Macé, G. Montaldo, M. Fink, and M. Tanter, "Viscoelastic and anisotropic mechanical properties of in vivo muscle tissue assessed by supersonic shear imaging," *Ultrasound Med. Biol.*, vol. 36, no. 5, pp. 789–801, 2010.

[21] S. Papazoglou, J. Rump, J. Braun, and I. Sack, "Shear wave group velocity inversion in MR elastography of human skeletal muscle," *Magn. Reson. Med.*, vol. 56, no. 3, pp. 489–497, 2006.

[22] C. Amador, M. Urban, S. Chen, and J. Greenleaf, "Shearwave dispersion ultrasound vibrometry (SDUV) on swine kidney," *IEEE Trans. Ultrason., Ferroelectr., Freq. Control*, vol. 58, no. 12, pp. 2608–2619, Dec. 2011.

[23] M. Tanter, D. Touboul, J. Gennisson, J. Bercoff, and M. Fink, "High-resolution quantitative imaging of cornea elasticity using supersonic shear imaging," *IEEE Trans. Med. Imag.*, vol. 28, no. 12, pp. 1881–1893, Dec. 2009.

[24] S. Kruse, G. Rose, K. Glaser, A. Manduca, J. Felmlee, C. Jack, jr, and R. Ehman, "Magnetic resonance elastography of the brain," *Neuroimage*, vol. 39, no. 1, p. 231, 2008.

[25] M. Green, L. Bilston, and R. Sinkus, "In vivo brain viscoelastic properties measured by magnetic resonance elastography," *NMR Biomed.*, vol. 21, no. 7, pp. 755–764, 2008.

[26] U. Hamhaber, I. Sack, S. Papazoglou, J. Rump, D. Klatt, and J. Braun, "Three-dimensional analysis of shear wave propagation observed by in vivo magnetic resonance elastography of the brain," *Acta Biomaterialia*, vol. 3, no. 1, pp. 127–137, 2007.

[27] J. O'Neill, *Musculoskeletal Ultrasound: Anatomy and Technique*. New York: Springer, 2008.

[28] M. Dresner, G. Rose, P. Rossman, R. Muthupillai, A. Manduca, and R. Ehman, "Magnetic resonance elastography of skeletal muscle," *J. Magn. Reson. Imag.*, vol. 13, no. 2, pp. 269–276, 2001.

[29] S. Bensamoun, S. Ringleb, L. Littrell, Q. Chen, M. Brennan, R. Ehman, and K. An, "Determination of thigh muscle stiffness using magnetic resonance elastography," *J. Magn. Reson. Imag.*, vol. 23, no. 2, pp. 242–247, 2005.

[30] I. Sack, J. Bernarding, and J. Braun, "Analysis of wave patterns in MR elastography of skeletal muscle using coupled harmonic oscillator simulations," *Magn. Reson. Imag.*, vol. 20, no. 1, pp. 95–104, 2002.

[31] R. Sinkus, M. Tanter, S. Catheline, J. Lorenzen, C. Kuhl, E. Sondermann, and M. Fink, "Imaging anisotropic and viscous properties of breast tissue by magnetic resonance-elastography," *Magn. Reson. Med.*, vol. 53, no. 2, pp. 372–387, 2005.

[32] S. Ringleb, S. Bensamoun, Q. Chen, A. Manduca, K. An, and R. Ehman, "Applications of magnetic resonance elastography to healthy and pathologic skeletal muscle," *J. Magn. Reson. Imag.*, vol. 25, no. 2, pp. 301–309, 2007.

[33] D. Klatt, S. Papazoglou, J. Braun, and I. Sack, "Viscoelasticity-based MR elastography of skeletal muscle," *Phys. Med. Biol.*, vol. 55, no. 21, p. 6445, 2010.

[34] J. Gennisson, S. Catheline, S. Chaffaï, and M. Fink, "Transient elastography in anisotropic medium: Application to the measurement of slow and fast shear wave speeds in muscles," *J. Acoust. Soc. Am.*, vol. 114, p. 536, 2003.

[35] J. Gennisson, C. Cornu, S. Catheline, M. Fink, and P. Portero, "Human muscle hardness assessment during incremental isometric contraction using transient elastography," *J. Biomechan.*, vol. 38, no. 7, pp. 1543–1550, 2005.

[36] K. Hoyt, T. Kneezel, B. Castaneda, and K. Parker, "Quantitative sonoelastography for the in vivo assessment of skeletal muscle viscoelasticity," *Phys. Med. Biol.*, vol. 53, no. 15, pp. 4063–4063, 2008.

[37] M. Urban, S. Chen, and J. Greenleaf, "Error in estimates of tissue material properties from shear wave dispersion ultrasound vibrometry," *IEEE Trans. Ultrason., Ferroelectr., Freq. Control*, vol. 56, no. 4, pp. 748–758, Apr. 2009.

[38] S. J. Hsu, M. L. Palemri, K. R. Nightingale, S. A. McAleavey, J. D. Dahl, and G. E. Trahey, "Shear wave anisotropy imaging," in *Proc. IEEE Ultrason. Symp.*, 2003, vol. 2, pp. 1090–1093.

[39] J. Bercoff, R. Sinkus, M. Tanter, and M. Fink, "3d ultrasound-based dynamic and transient elastography: First in vitro results," in *Proc. 2004 IEEE Ultrason. Symp.*, 2004, vol. 1, pp. 28–31.

[40] W. M. Lai, D. Rubin, and E. Krempl, *Introduction to Continuum Mechanics*, 3rd ed. Burlington, MA: Elsevier, 1996.

[41] M. Musgrave, "The propagation of elastic waves in crystals and other anisotropic media," *Rep. Progress Phys.*, vol. 22, pp. 74–96, 1959.

[42] J. Dellinger, "Anisotropic seismic wave propagation," Ph.D. dissertation, Stanford Univ., Stanford, CA, 1991.

[43] T. Deffieux, G. Montaldo, M. Tanter, and M. Fink, "Shear wave spectroscopy for in vivo quantification of human soft tissues visco-elasticity," *IEEE Trans. Med. Imag.*, vol. 28, no. 3, pp. 313–322, Mar. 2009.

[44] M. H. Wang, B. C. Byram, M. L. Palmeri, N. C. Rouze, and K. R. Nightingale, "On the precision of time-of-flight shear wave speed estimation in homog eneous soft solids: Initial results using a matrix array transducer," *IEEE Trans. Ultrason., Ferroelectr., Freq. Control*, vol. 60, no. 4, pp. 758–770, Apr. 2013.

[45] A. Pesavento, C. Perrey, M. Krueger, and H. Ermert, "A time-efficient and accurate strain estimation concept for ultrasonic elastography using iterative phase zero estimation," *IEEE Trans. Ultrason., Ferroelectr., Freq. Control*, vol. 46, no. 5, pp. 1057–1067, May 1999.

[46] M. Burlew, E. Madsen, J. Zagzebski, R. Banjavic, and S. Sum, "A new ultrasound tissue-equivalent material," *Radiology*, vol. 134, no. 2, pp. 517–520, 1980.

[47] M. L. Palmeri, M. H. Wang, J. J. Dahl, K. D. Frinkley, and K. R. Nightingale, "Quantifying hepatic shear modulus in vivo using acoustic radiation force," *Ultrasound Med. Biol.*, vol. 34, no. 4, pp. 546–558, 2008.

[48] M. Fischler and R. Bolles, "Random sample consensus: A paradigm for model fitting with applications to image analysis and automated cartography," *Commun. ACM*, vol. 24, no. 6, pp. 381–395, 1981.

[49] B. Horn, "Closed-form solution of absolute orientation using unit quaternions," *J. Opt. Soc. Am. A*, vol. 4, no. 4, pp. 629–642, 1987.

[50] M. Rana, G. Hamarneh, and J. Wakeling, "Automated tracking of muscle fascicle orientation in b-mode ultrasound images," *J. Biomechan.*, vol. 42, no. 13, pp. 2068–2073, 2009.

[51] H. Zhao and L. Zhang, "Automatic tracking of muscle fascicles in ultrasound images using localized Radon transform," *IEEE Trans. Biomed. Eng.*, vol. 58, no. 7, pp. 2094–2101, Jul. 2011.

[52] A. Frangi, W. Niessen, K. Vincken, and M. Viergever, "Multiscale vessel enhancement filtering," in *Med. Image Comput. Comput.-Assist. Intervent.*, 1998, pp. 130–137.

[53] K. Topp and W. O'Brien, Jr, "Anisotropy of ultrasonic propagation and scattering properties in fresh rat skeletal muscle in vitro," *The J. Acoust. Soc. Am.*, vol. 107, p. 1027, 2000.

[54] M. L. Palmeri, A. C. Sharma, R. R. Bouchard, R. W. Nightingale, and K. R. Nightingale, "A finite-element method model of soft tissue response to impulsive acoustic radiation force," *IEEE Trans. Ultrason., Ferroelectr., Freq. Control*, vol. 52, no. 10, pp. 1699–1712, Oct. 2005.

[55] H. Zhao, P. Song, M. Urban, R. Kinnick, M. Yin, J. Greenleaf, and S. Chen, "Bias observed in time-of-flight shear wave speed measurements using radiation force of a focused ultrasound beam," *Ultrasound Med. Biol.*, vol. 37, no. 11, pp. 1884–1892, 2011.